A&A, 710, A51 (2026)
https://doi.org/10.1051/0004-6361/202659430

Astronomy & Astrophysics

Forward modeling solar spectra onto Doppler images of λ And

Ö. Adebali[1,2,⋆] and A. G. M. Pietrow[1,⋆]

[1] Leibniz-Institut für Astrophysik Potsdam (AIP), An der Sternwarte 16, 14482 Potsdam, Germany
[2] Institut für Physik und Astronomie, Universität Potsdam, 14476 Potsdam, Germany

Received 12 February 2026 / Accepted 27 April 2026

ABSTRACT

Context. Due to their high chromospheric activity and photometric variability, RS CVn-type binaries are ideal laboratories for studying stellar surface structures and the corresponding stellar activity relations. However, the atmospheric nature of their primary evolved components (luminosity classes III–IV) are more complex than those of main-sequence stars. Additionally, detailed models are still lacking for the sub(giant) systems. Therefore, comparative techniques represent the most effective approach for probing the connection between chromospheric emission and surface structures.

Aims. Using the Doppler images of λ And, we investigated whether surface temperature information can be reversed to create its activity parameters by feeding a toy model solar spectra based on surface images. At the same time, we examined whether spot contributions alone are sufficient to explain the observed activity modulation of the RS CVn star λ And while quantifying the differences with the actual observations of this star obtained simultaneously with the Doppler images we used.

Methods. Due to a lack of publicly available starspot models for its stellar type, we adopted the observed solar spectra as the only available approximation of λ And's spots. These spectra were injected into a sequence of a full-disk temperature map derived from Doppler imaging that represents a full stellar rotation. These disks were then forward modeled into disk-integrated spectra with the Numerical Empirical Sun-as-a-star Integrator (NESSI). This experiment was performed on three photospheric lines (Fe I 6173 Å, Fe I 6301 Å, and K I 7699 Å) and four chromospheric lines (Hα, Ca II H&K, and Ca II 8542 Å). Finally, we used these spectra to calculate the radial velocities and chromospheric emissions diagnostics, which in turn were compared to the original photospheric and chromospheric characteristics of the star.

Results. Despite the very different stellar structures and atmospheric stratification between λ And and the Sun, we show that the chromospheric emissions produced by our toy model largely follow the same trend as the original observations of λ And. This indicates that the modulation of the chromospheric activity is dominated by magnetic activity associated with the active regions with dark spots. In addition, the differences in the emission amplitudes quantify the different chromospheric heating mechanisms for these two very different types of stars.

Conclusions. Using this approach, we show that even with simplified assumptions the spectral behavior of λ And can be qualitatively reproduced. Toy models such as the one presented in this work make an additional dimension available by providing a relation between the surface structures and chromospheric emissions. Such models also help in developing a further understanding of the heating mechanisms of these active giants through comparative techniques, where in this case the spot activity seemingly modulates the chromospheric signal and can explain the bulk of its variations over a rotation.

Key words. stars: activity – stars: atmospheres – stars: chromospheres – stars: imaging – starspots

1. Introduction

Spots are among the most easily identifiable examples of magnetic field inhomogeneities in stellar atmospheres. They are characterized by a dark umbra surrounded by a brighter but still dark penumbra (Solanki 2003). The spectral profiles of spots are shaped by markedly different local thermodynamic and magnetic conditions (e.g., Avrett et al. 2015; Kuckein et al. 2021). Nevertheless, when modeling spots on stars other than the Sun, these structures are usually reduced to uniform surface elements that share the same atmospheric stratification as the quiet photosphere, aside from a decrease in effective temperature. (e.g. Chakraborty et al. 2024; Petit dit de la Roche et al. 2024; Cristo et al. 2025). State-of-the-art magnetohydrodynamic simulations of starspots are currently being developed (e.g. Smitha et al. 2025) but are not yet widely implemented.

Studying these features provides insight into the connection between the activity of different atmospheric layers, such as the photosphere and the chromosphere (Strassmeier 2009). The Sun displays relatively small spots, typically up to about 100 MSH[1], whereas spots several orders of magnitude larger and filling factors of tens of percent have been reported on other stars. However, it is unclear whether these are singular monolithic spots or rather clumps of smaller unresolved spots (Solanki & Unruh 2004).

The primary components of RS CVn-type binary systems in particular tend to have very large starspots and filling factors as well as excessive chromospheric activity. These characteristics make them appropriate targets for spot detection and observation. These systems have been extensively studied over the past fifty years, beginning with Hall (1972) and later through the development of the Doppler imaging technique (Vogt & Penrod 1983), which provided a more detailed approach to studying these giant activity laboratories. In the years following, subsequent studies provided more information on different systems, enabling better understanding of various aspects of stellar

⋆ Corresponding authors: oadebali@aip.de; apietrow@aip.de

[1] Millionths of a solar hemisphere.

activity, including stellar differential rotation, activity cycles, magnetic fields, and stellar winds (see e.g., Strassmeier 2009; Alvarado-Gómez et al. 2016).

However, these higher activity levels present their own limitations. For example, it becomes more difficult to obtain more precise and accurate results for stellar parameters such as mass and radius. Radial velocity (RV) is another parameter that is highly affected by large spots, which can contaminate and even mimic the RV signal originating from orbiting exoplanets (e.g., Moulds et al. 2013; Bortle et al. 2021; Simpson et al. 2022). Additionally, other activity features, such as flares (Reiners 2009; Pietrow et al. 2024) and faculae (Cristo et al. 2025) have also been shown to create perturbations in RV signals.

λ Andromedae (λ And) is a famous RS CVn system displaying massive spots, and it has been studied for over a century (Donati et al. 1995; Parks et al. 2021; Ó Fionnagáin et al. 2021). In a recent work by Adebali et al. (2025), enhanced chromospheric activity was investigated, and the authors showed varying activity modulation from 10% to 50% within a time span of about 10 rotations for different activity indicators such as Ca II H&Kand Hα as well as the Ca II infrared triplet (IRT). Moreover, the RV analysis showed a long-term modulation with an amplitude of 300 m s^{-1}.

Although many of the aforementioned techniques provide detailed results for inferred quantities of λ And, more detailed and comparative methods are lacking to understand the activity imprints of its surface structures. For this reason, it is important to not only employ different techniques but also test them in robust ways. In this work, we plan to do exactly this by creating a toy model of λ And based on the Doppler imaging map from Adebali et al. (2025), which in turn can be forward modeled into a spectral time series for different lines that can then be used for further activity analysis. We note that the surface images of λ And were obtained from a dataset with a very high spectral resolution (R $\sim$ 250 000) and signal-to-noise ratio (reaching up to 1000). The observations cover a total of 40 days for the primary star of the system (P_{rot} = 54 days) with well-distributed sampling. We therefore assume that despite the small rotational broadening, the reconstructed surface structures represent the magnetic activity of the star reasonably well (see details in Adebali et al. 2025).

To perform this spectral synthesis, we used sunspot spectra obtained from different regions of the sunspots and their surrounding areas. These spectra were then used as input for the Doppler images. In practice, we mapped the temperature distribution derived for λ And onto the solar surface and searched for the resulting differences in the activity indicators. A more detailed description of this procedure is provided in Sect. 2.

In previous work, traditional approaches were used to model activity indicators such as Ca II H&K and Ca II IRT for different stars by employing stellar template spectra (Mittag et al. 2013; Martin et al. 2017). However, these methods may fail for RS CVn systems for two main reasons. First, the determination of stellar parameters for RS CVn stars, such as visual magnitudes, is often uncertain. Because the primary components of these systems exhibit large starspots, their observed stellar parameters can be significantly affected by stellar activity (see Adebali et al. 2026). Second, these approaches often rely on simplified approximations when modeling chromospheric emission (e.g., Han et al. 2025). In this work, we address this limitation by using direct observations of spots from the Sun to represent chromospheric contributions.

In the following sections, we introduce our stellar-disk modeling and then explain our activity analysis both in photospheric, via the RV regime, and chromospheric layers. In the conclusions, we investigate the differences between the activity signatures created by our toy model and the actual observations of λ And.

2. Stellar disk modeling with `NESSI`

The toy model was generated using the Numerical Empirical Sun-as-a-star Integrator (NESSI; Pietrow & Pastor Yabar 2024; De Wilde et al. 2025), which employs a radial polar sampling scheme that traces a one-dimensional spiral across the stellar disk. Each point along this spiral corresponds to a surface element with a specific area to which an appropriate spectrum can be assigned. NESSI functions in a similar manner to the Spot Oscillation And Planet (SOAP; Cristo et al. 2025) code, but it is optimized for detailed surface features and empirical data, making it ideal for this use case.

NESSI works by selecting a "disk center" spectrum that spans a given spectral range. This spectrum is then modulated with a wavelength-dependent limb-darkening curve, such as those given by Pietrow et al. (2023), Canocchi et al. (2024), and Ellwarth et al. (2023). Then, a rotational profile as described in Lößnitz et al. (2025) is applied to the disk at a given heliographic latitude[2] (in this case, 20°) and a rigid rotation of 7.0 km/s is introduced (Adebali et al. 2025), as the differential rotation rate is assumed to be negligible for this star and the Doppler method is not sensitive to differential rotation over just one rotation. Thus, the main reason why we did not consider differential rotation is that our observations do not cover multiple rotations, contrary to the case of, for example, KU Peg (Kővári et al. 2016).

For this work, we slightly modified the method, as we used the Doppler imaging map from Adebali et al. (2025) to create intensity-based masks that separate the map into three thresholds, namely the quiet-Sun, penumbra, and umbra. We applied these maps to the NESSI grid and filled each of the three masks with spectra of the corresponding regions, as explained below. The grid was then processed normally with limb darkening and rotation. We assumed that spots and the quiet Sun have the same limb-darkening curves, despite evidence suggesting otherwise (e.g., Rödberg 1966; Cretignier et al. 2024). However, currently no empirical or synthetic limb-darkening atlases exist for sunspots apart from a few individual lines. Based on preliminary results from Pietrow et al. (in prep.), we estimate that the difference in limb darkening remains below 5% for the majority of the time a sunspot spends crossing the disk. Only within the last ~2% of the solar radius near the limb does this discrepancy increase to around 15%. For this reason, we consider the effect to be negligible compared to the uncertainties introduced by other assumptions in this work.

At present, neither the Sun nor other stellar types have a publicly available database of physically consistent synthetic spot spectra. Empirical spot spectra are also rare and fragmented, with the only available resource being a low signal-to-noise umbral atlas spanning wavelengths from 6642 Å to 11 230 Å (Wallace et al. 1999). However, a self-consistent sunspot atlas is expected to become available in the near future with the commissioning of the Paranal solar ESPRESSO Telescope (Santos et al. 2025). Therefore, we used the next best thing in the form of empirical spot spectra observed with the Swedish 1-m Solar Telescope (SST; Scharmer et al. 2003). These observations offer a high spatial (~0.058 arcseconds/pixel) and spectral

[2] This is equal to the inclination of rotation value but with the zero defined at the solar disk center, meaning that $B_0 = 90° - i$, where B_0 is the heliographic latitude and i is the inclination of rotation.

Table 1. Swedish Solar Telescope observations used in this study.

Archive ID	NOAA	Date (UTC)	X (″)	Y (″)	μ	T_U (K)	T_P (K)	Spectral lines	
456	13 395	2023-08-06 08:51–08:58	–655	169	0.71	4581	6168	K I Fe I Ca II	7699 Å 6173 Å 8542 Å
416	13 433	2023-09-15 08:38–09:08	–454	355	0.80	4517	6078	Fe I Ca II H Ca II K	6301 Å 3968 Å 3933 Å
423	13 468	2023-10-20 09:05–10:51	–380	–247	0.88	4549	6197	Hα	6563 Å

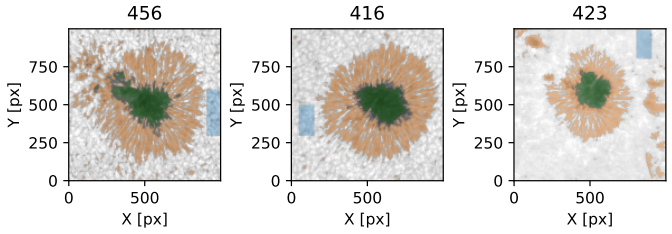

Fig. 1. High-resolution sunspot images corresponding to the datasets shown in Table 1. The highlighted quiet Sun (blue), penumbra (orange), and umbra (green) regions were obtained with intensity thresholds. Pixels within the highlighted regions have been averaged into their respective spectral profile. The images are of the continuum left of Fe I 6173 Å, Fe I 6302 Å, and the Hα pseudo-continuum. All figures have an observed resolution of 0.058″/pixel.

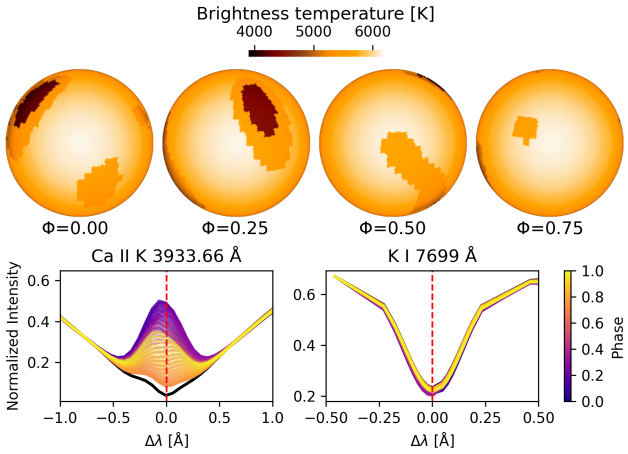

Fig. 2. Simulated stellar disks and their profiles. Top: four resolved NESSI disk brightness temperature maps based on the provided Doppler imaging map with distinct umbra, penumbra, and quiet Sun regions as well as applied limb darkening. From left to right, the phases are 0, 0.25, 0.5, and 0.75. Bottom: resulting spectra for Ca II K and K I 7699 Å for all phases (colored) and the disk with no spots (black). The red dashed lines denote the rest wavelength of the line.

(R ∼ 150 000) resolution over a relatively small spectral range of about 1 Å. The data used come from the publicly available SST archive[3] and were observed with both the CRisp Imaging SpectroPolarimeter (CRISP; Scharmer et al. 2008) and the CHROMospheric Imaging Spectrometer (CHROMIS; Scharmer 2017). Unfortunately, there is no single sunspot observation that covers all the spectral lines of interest. For this reason, multiple observations were combined (see Table 1 and Fig. 1). As a result, our spectra do not sample the same sunspot regions and were recorded at different locations on the solar disk. While this introduces obvious limitations in terms of self-consistency, such as variations in spectral width and depth with heliocentric angle μ (e.g. Pietrow et al. 2023, 2026), we argue that the resulting average umbral and penumbral spectra are still an adequate approximation for the present study. This is because Doppler shifts can be removed and intensities (of the order of 10% due to limb darkening) can be rescaled. Moreover, the remaining profile differences are expected to behave smoothly with μ between the different types of spectra. The intensity calibration was performed using the `get_calibration` function from the `ISPy` package (Díaz Baso et al. 2021). This routine fits the continuum, where available, or otherwise the far wings of the spectral line using the spectral atlas of Neckel & Labs (1984) applied to the empty-disk observations and subsequently transfers this calibration to all remaining spectra. Before fitting the atlas, spectra are convolved with the SST instrumental profile and include a rotational broadening term following Eq. (18.14) of Gray (2022). The line core was excluded from the fit due to contamination by activity-related signals, which are present in this and most other atlases (Hanassi-Savari et al. 2025; Pietrow 2026). Additionally, by comparing the blackbody or brightness temperatures of the three spots in the 6173 Å continuum using data from the Helioseismic and Magnetic Imager (Scherrer et al. 2012) on board the Solar Dynamics Observatory (Pesnell et al. 2012), we found that their temperatures are very similar. The median umbral brightness temperatures of each spot cluster within about 30 K of 4550 K, while the penumbral temperatures fall within roughly 100 K of 6150 K. The quiet Sun surface temperature at this height in the photosphere is 6700 K (e.g., Fontenla et al. 1993, model C).

For each sunspot observation, we manually selected an intensity threshold that could be used to split the image into umbra, penumbra, and quiet Sun pixels (see Fig. 1 and Fig. A.1), which were then averaged and shifted to remove any Doppler shifts (see Fig. A.2). These profiles were then injected into the NESSI disk, as explained above, and the process was repeated for the 60 masks created from the Doppler imaging map for each line. These grids were then numerically integrated to create synthetic stellar spectra of the disk in question (see Fig. 2). An "empty" (nonspotted) disk was created for each line to use as the "null spectrum" in the Doppler and RV analysis.

[3] https://dubshen.astro.su.se/sst_archive/

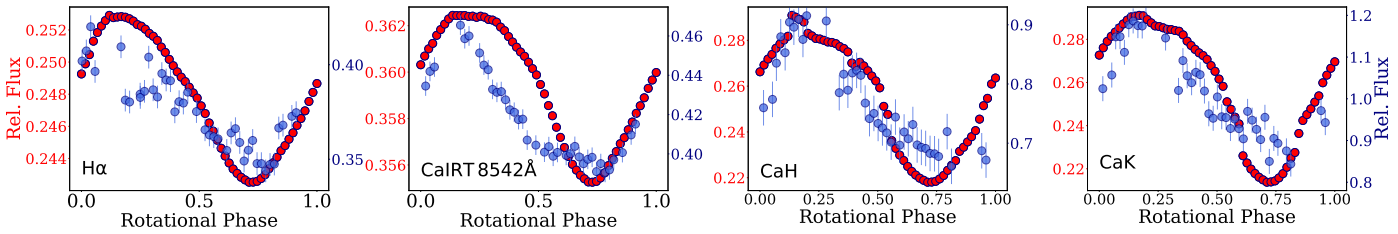

Fig. 3. Chromospheric emission variability. Emissions from Hα, Ca II 8542 Å, and Ca II H&K are plotted against the rotational phase of the star as modeled (red) and observed (blue) values. The scale differences between the modeled and observed values are indicated with red and blue y-axis colors, respectively. The emissions are plotted as fluxes relative to the continuum.

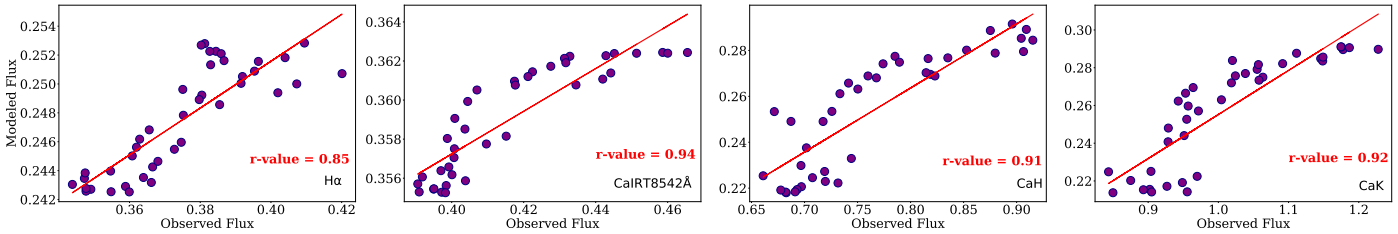

Fig. 4. Flux correlations between the observed and the modeled values. The red line shows the linear fit for the given chromospheric emissions. The r-values indicate the spearman correlation coefficients for the given measurements.

3. Activity analysis

To compare activity levels, we examined changes in line-core intensity and RV calculations over one rotation of our toy model. First, we examined how surface structures affect the emissions at different chromospheric layers. Then, to make a broader comparison with the actual observations, we calculated the activity-induced RV changes, that is, the activity imprints at the photospheric layer.

3.1. Chromospheric emissions

We measured the line-core emission fluxes in the 1-Å region centered around the line cores of Ca II H&K, Hα, and Ca II IRT 8542 Å. Relative flux measurements were obtained by integrating the area between the spectrum and the zero point. Unit conversions and further discussion for radiative loss calculations can be found in Adebali et al. (2025) and Järvinen & Strassmeier (2025). After calculating the emission fluxes (Fig.3), we fit a sinusoidal function to the phase-dependent relative flux values via the χ^2 routine of the `scipy` package (Virtanen et al. 2020). Based on our fits, we determined that the maximum emission excess for Ca II H&K, which is about $\simeq$ 30%. These two emission indicators are the ones with the highest modulation amplitudes. Hα fluxes follow them with a much lower modulation rate, about 5%. The lowest modulation rate was determined for Ca II IRT 8542 Å, where the amplitude changes over a rotation with a rate of about 2% of the minimum value of the calculated fluxes. At the same time, we note that in all four cases the simulated activity signal is weaker than that of the λ And, with the biggest difference coming from Ca II H&K, then Hα, and finally Ca II IRT 8542 Å. This differential response in chromospheric lines is consistent with that reported by Pietrow et al. (2024), and the references therein. The discrepancy between the shape of each curve and the original data, most clearly visible in Fig. 3, correlates with the degree to which the average penumbral profile resembles that of the umbra (see Fig. A.2). The largest scatter was found in the Hα line, where the penumbral profile is nearly indistinguishable from that of the quiet Sun, resulting in the lowest correlation coefficient (see Fig. 4). This lack of contrast significantly reduces the penumbral contribution to the stellar surface, effectively giving greater weight to the darker umbral component and thereby altering the recovered line profile. The Ca II IRT 8542 Å umbral profile has a similar issue, where it has an equal depth to the surrounding quiet Sun but also shows an asymmetrical broadening. This broadening could introduce an asymmetry in response to penumbral patches on the left and right sides of the disk, which indeed seems to be the case in the second panel of Fig. 3, where a reduced response is seen when the spot is on the right side of the disk.

The correlation between the integrated flux of the model and the observed spectra is shown in Fig. 4. A clear correlation is present at low activity levels, while a distinct deviation appears at the highest values. This behavior likely reflects our assumption where large spots in the Doppler map are treated as monolithic structures. Interestingly, the Hα line does not seem to show this break, potentially making it the best line for this type of modeling.

3.2. Radial velocities

While computing the RV data points, we used the null spectrum calculated by NESSI as a model spectrum and then obtained the RV points by using the cross-correlation function. Since the stellar parameters are the same for each spectrum, the only difference for each individual line should come from the surface structures imprinting on line core shifts and thus on RV values. As shown in Fig. 5, phase-dependent RV modulations create similar patterns with different amplitudes for the used photospheric lines. The highest modulation was calculated for the iron line at 6302 Å with an amplitude of $\simeq$320 m s^{-1}, and the lowest modulation was obtained by K I 7699 Å at around $\simeq$200 m s^{-1}. We attribute these differences to two different effects, chromaticity and sensitivity of the lines to the temperature changes, which are formed in the given wavelength regions. The first effect has been discussed by Larue et al. (2025), who explain that in the blue spectral regions, the activity effects

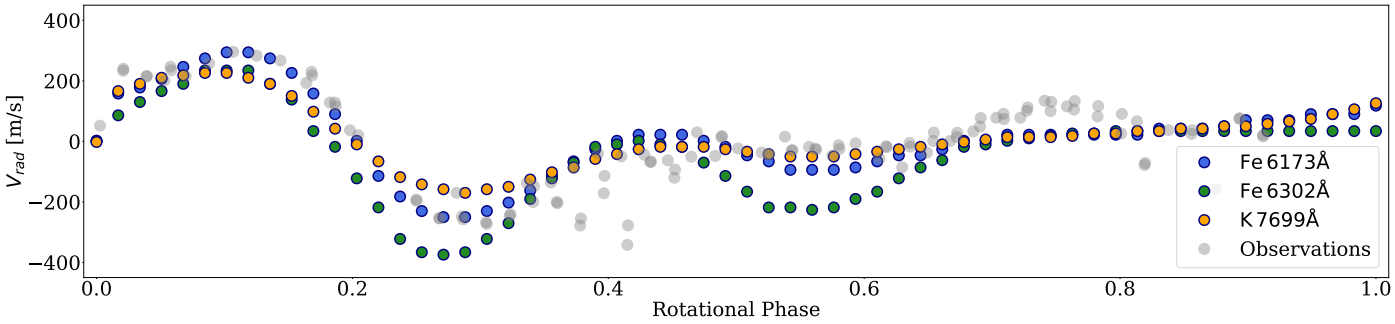

Fig. 5. Radial velocity evolution over the rotational phase. The blue, green, and orange circles indicate Fe I 6173 Å, Fe I 6302 Å, and K I 7699 Å, respectively. The gray dots show the actual observations.

on RVs are observed more prominently. Furthermore, a second modulation appears between phases 0.4–0.6 with an amplitude of 60 m s^{-1} and 120 m s^{-1} for Fe I 6173 Å and Fe I 6302 Å, respectively. The K I 7699 Å shows a smaller amplitude of ≃20 m s^{-1}.

4. Discussion

Using the NESSI code, we constructed a toy model of λ And based on the Doppler imaging map of Adebali et al. (2025). We synthesized disk-integrated spectra from this surface map and compared them to the actual observations of the star that were simultaneously obtained with the Doppler images we used. This allowed us to evaluate the origins of the chromospheric emissions of λ And and provide a solar-stellar connection from a different perspective.

Upon examining the activity modulation (as shown in Fig. 3), we found that the overall variability patterns are qualitatively well reproduced with spot-related activity alone despite the mismatches in the absolute flux levels and its modulation amplitude over one rotation. As these two stars demonstrate very different properties and we were only matching their temperature differences on their photospheres, this is very much in line with expectations. On the other hand, λ And is very active in its chromospheres, which already categorizes this system in the group of RS CVn-type binaries. The fact that Ca II H&K lines show the highest modulation both in actual observations and in our toy model indicates that upper chromospheres of both stars are heated in relatively the same way, although the column density and the stratification of their atmospheres are vastly different. As shown in Fig. 3, the actual observations demonstrate a modulation amplitude of 35% on average for the upper chromosphere, and it is slightly higher than our results (30%). The percentile difference for Hα is about 25% in the observations, and for Ca II IRT 8542 Å this value is about 20%. As shown in the upper chromosphere, the flux amplitudes inferred from these lines point out that λ And has more efficient heating in the lower and middle chromosphere than our toy model as well. In addition, the assumption of monolithic spots may be incorrect, and these regions may in fact be composed of smaller spots and surrounding plages and may experience complex small-scale interaction of magnetic fields, which would lower the contrast but raise the activity signal.

The RV modulations are more closely aligned with each other when compared with the chromospheric variations, even though the spectra originate from different spots. Concurrently, this is expected since the RV variations depend more strongly on the filling factors of the spots as well as on the spot temperatures. The temperature contrast, together with the size and the locations of the spots, cause asymmetries for the observed parts of the stellar-disk. This effect creates considerable difficulty while obtaining RV values (see e.g., Boisse et al. 2011). Although we compared different spots with different temperature contrasts for both stars, since we used the same surface structure from the Doppler imaging map, the observations are better correlated with the results from our toy model. However, when we examined the individual lines, the details became more prominent. The amplitude of the potassium line is about half that of the iron lines, which we interpret as the chromaticity effect on the RVs (Larue et al. 2025). The average maximum RV amplitude calculated from these three lines is ≃250m s^{-1}, which is lower than the observed value of ≃300 m s^{-1} (Adebali et al. 2025). We note that the RV values observed by Adebali et al. (2025) were obtained on the basis of 500 lines in a region between 4800 and 5400 Å. Therefore, although the surface structures were introduced in the same way as in the Doppler images, the RV modulation based on our model is about 20% less than the observed values, which is an underestimation in contrast to the model side. However, the RV observations are also affected by instrumental noise and different surface effects (e.g., convective blueshift) that are not possible to resolve in the Doppler image of λ And.

In summary, from the chromospheric indices, we find a good match in shape but an underestimation in magnitude. From the photospheric RVs, we find a match in pattern but an underestimation in magnitude. This implies that our spots do not adequately reproduce the active regions on λ And. Also, perhaps contradictorily, this model expects darker spots in the photosphere and more active areas in the chromosphere. This may be explained by plages, as based on solar observations, we know that plages can be close to invisible at the disk center when seen in the photosphere while presenting as bright in the chromosphere.

5. Conclusion

For the experiment presented in this paper, we used publicly available tools to construct synthetic spectra representative of a G8-type giant star. However, present stellar-atmosphere modeling capabilities do not yet permit the computation of spectra from a realistic atmospheric model tailored to this star. As a result, solar spectra were used as a proxy. Although many of the observed spectral properties were reproduced, several discrepancies remained between the synthetic and observed spectra, which likely arise from differences in the atmospheric structure and parameters between the Sun and λ Andand the absence of plages and other bright structures in our model. However, the modulation of the RVs and activity indices is well aligned with

the actual and simultaneous observations. This leads to the conclusion that despite their limitations, toy models such as the one presented here retain a significant diagnostic value. In particular, our results indicate that only spot spectra can account for the significant portion of the relative modulation of chromospheric emissions at different layers for this system without requiring the inclusion of bright plages. However, at the same time, such features might be needed to better reproduce the magnitude of these modulations. Especially, for the actual observations of λ And, the spots seem much more efficient for creating the mechanism of heating for the chromospheric layers than the sunspot observations we used for this experiment. Also, for the first time, we have determined that the main chromospheric emission source of λ And is its huge spot regions, which we followed through its Doppler images.

Based on the given comparisons above, between the Sun and λ And, we plan to quantify the activity tracers of a broader sample of stars. Future work will focus on expanding this analysis, including solar-like and fast-rotating systems (e.g., EK Dra; Järvinen et al. 2018; Görgei et al. 2026), and more RS CVn-type systems (e.g., HR 7275; Adebali et al. 2026) through the use of developing and more advanced spectral-synthesis methods using more lines and a more realistic atmosphere.

Acknowledgements. We thank an anonymous referee for their constructive comments that significantly improved the quality of this work. AP is supported by the Deutsche Forschungsgemeinschaft (DFG) project number PI 2102/1-1. ÖA acknowledges the insightful critiques from D. Gruner, J. Alvarado-Gomez, M. Weber and K. G. Strassmeier. In this work, we heavily used `python3` libraries; `astropy` (Astropy Collaboration 2013, 2018, 2022), `numpy` (Harris et al. 2020) `scipy` (Virtanen et al. 2020), and ISPy (Díaz Baso et al. 2021). DeepL Write was used in copy editing (spelling, grammar, and readability) of the manuscript.

References

Adebali, Ö., Strassmeier, K. G., Ilyin, I. V., et al. 2025, A&A, 695, A89
Adebali, Ö., Weber, M., Strassmeier, K. G., et al. 2026, A&A, 706, A179
Alvarado-Gómez, J. D., Hussain, G. A. J., Cohen, O., et al. 2016, A&A, 594, A95
Astropy Collaboration (Robitaille, T. P., et al.) 2013, A&A, 558, A33
Astropy Collaboration (Price-Whelan, A. M., et al.) 2018, AJ, 156, 123
Astropy Collaboration (Price-Whelan, A. M., et al.) 2022, ApJ, 935, 167
Avrett, E., Tian, H., Landi, E., Curdt, W., & Wülser, J.-P. 2015, ApJ, 811, 87
Boisse, I., Bouchy, F., Hébrard, G., et al. 2011, A&A, 528, A4
Bortle, A., Fausey, H., Ji, J., et al. 2021, AJ, 161, 230
Canocchi, G., Lind, K., Lagae, C., et al. 2024, A&A, 683, A242
Chakraborty, H., Lendl, M., Akinsanmi, B., et al. 2024, A&A, 685, A173
Cretignier, M., Pietrow, A. G. M., & Aigrain, S. 2024, MNRAS, 527, 2940
Cristo, E., Faria, J. P., Santos, N. C., et al. 2025, A&A, 702, A84
De Wilde, M., Pietrow, A. G. M., Druett, M. K., et al. 2025, A&A, 700, A275
Díaz Baso, C. J., Vissers, G., Calvo, F., et al. 2021, https://doi.org/10.5281/zenodo.5608441
Donati, J. F., Henry, G. W., & Hall, D. S. 1995, A&A, 293, 107
Ellwarth, M., Schäfer, S., Reiners, A., & Zechmeister, M. 2023, A&A, 673, A19
Fontenla, J. M., Avrett, E. H., & Loeser, R. 1993, ApJ, 406, 319
Görgei, A., Kriskovics, L., Vida, K., et al. 2026, A&A, 706, A54
Gray, D. F. 2022, The observation and analysis of stellar photospheres (Cambridge: Cambridge University Press)
Hall, D. S. 1972, PASP, 84, 323
Han, H., Wang, S., Li, X., Zheng, C., & Liu, J. 2025, ApJ, 984, 2
Hanassi-Savari, F., Pietrow, A. G. M., Druett, M. K., Cretignier, M., & Ellwarth, M. 2025, A&A, 702, A97
Harris, C. R., Millman, K. J., van der Walt, S. J., et al. 2020, Nature, 585, 585
Järvinen, S. P., & Strassmeier, K. G. 2025, A&A, 698, A93
Järvinen, S. P., Strassmeier, K. G., Carroll, T. A., et al. 2018, A&A, 620, A162
Kővári, Z., Künstler, A., Strassmeier, K. G., et al. 2016, A&A, 596, A53
Kuckein, C., Balthasar, H., Quintero Noda, C., et al. 2021, A&A, 653, A165
Larue, P., Delfosse, X., Carmona, A., et al. 2025, A&A, 701, A216
Lößnitz, E. J., Pietrow, A. G. M., Chakraborty, H., et al. 2025, A&A, 703, A187
Martin, J., Fuhrmeister, B., Mittag, M., et al. 2017, A&A, 605, A113
Mittag, M., Schmitt, J. H. M. M., & Schröder, K.-P. 2013, A&A, 549, A117
Moulds, V. E., Watson, C. A., Bonfils, X., et al. 2013, MNRAS, 430, 1709
Neckel, H., & Labs, D. 1984, Sol. Phys., 90, 205
Ó Fionnagáin, D., Vidotto, A. A., Petit, P., et al. 2021, MNRAS, 500, 3438
Parks, J. R., White, R. J., Baron, F., et al. 2021, ApJ, 913, 54
Pesnell, W. D., Thompson, B. J., & Chamberlin, P. C. 2012, Sol. Phys., 275, 3
Petit dit de la Roche, D. J. M., Chakraborty, H., Lendl, M., et al. 2024, A&A, 692, A83
Pietrow, A. G. M. 2026, Open J, Astrophys., 9, 58273
Pietrow, A. G. M., & Pastor Yabar, A. 2024, in IAU Symposium, 365, Dynamics of Solar and Stellar Convection Zones and Atmospheres, eds. A. V. Getling, & L. L. Kitchatinov, 389
Pietrow, A. G. M., Kiselman, D., Andriienko, O., et al. 2023, A&A, 671, A130
Pietrow, A. G. M., Cretignier, M., Druett, M. K., et al. 2024, A&A, 682, A46
Pietrow, A. G. M., Kuckein, C., Verma, M., et al. 2026, A&A, 705, A116
Reiners, A. 2009, A&A, 498, 853
Rödberg, H. 1966, Nature, 211, 394
Santos, N. C., Cabral, A., Leite, I., et al. 2025, The Messenger, 194, 21
Scharmer, G. 2017, in SOLARNET IV: The Physics of the Sun from the Interior to the Outer Atmosphere, 85
Scharmer, G. B., Bjelksjo, K., et al. 2003, SPIE Conf. Ser., 4853, 341
Scharmer, G. B., Narayan, G., Hillberg, T., et al. 2008, ApJ, 689, L69
Scherrer, P. H., Schou, J., Bush, R. I., et al. 2012, Sol. Phys., 275, 207
Simpson, E. R., Fetherolf, T., Kane, S. R., et al. 2022, AJ, 163, 215
Smitha, H. N., Shapiro, A. I., Witzke, V., et al. 2025, ApJ, 978, L13
Solanki, S. K. 2003, A&A Rev., 11, 153
Solanki, S. K., & Unruh, Y. C. 2004, MNRAS, 348, 307
Strassmeier, K. G. 2009, A&A Rev., 17, 251
Virtanen, P., Gommers, R., Oliphant, T. E., et al. 2020, Nat. Methods, 17, 261
Vogt, S. S., & Penrod, G. D. 1983, PASP, 95, 565
Wallace, L., Livingston, W. C., Bernath, P. F., & Ram, R. S. 1999, NSO Technical Report #99-001 (Tucson: National Solar Observatory)

Appendix A: Figures

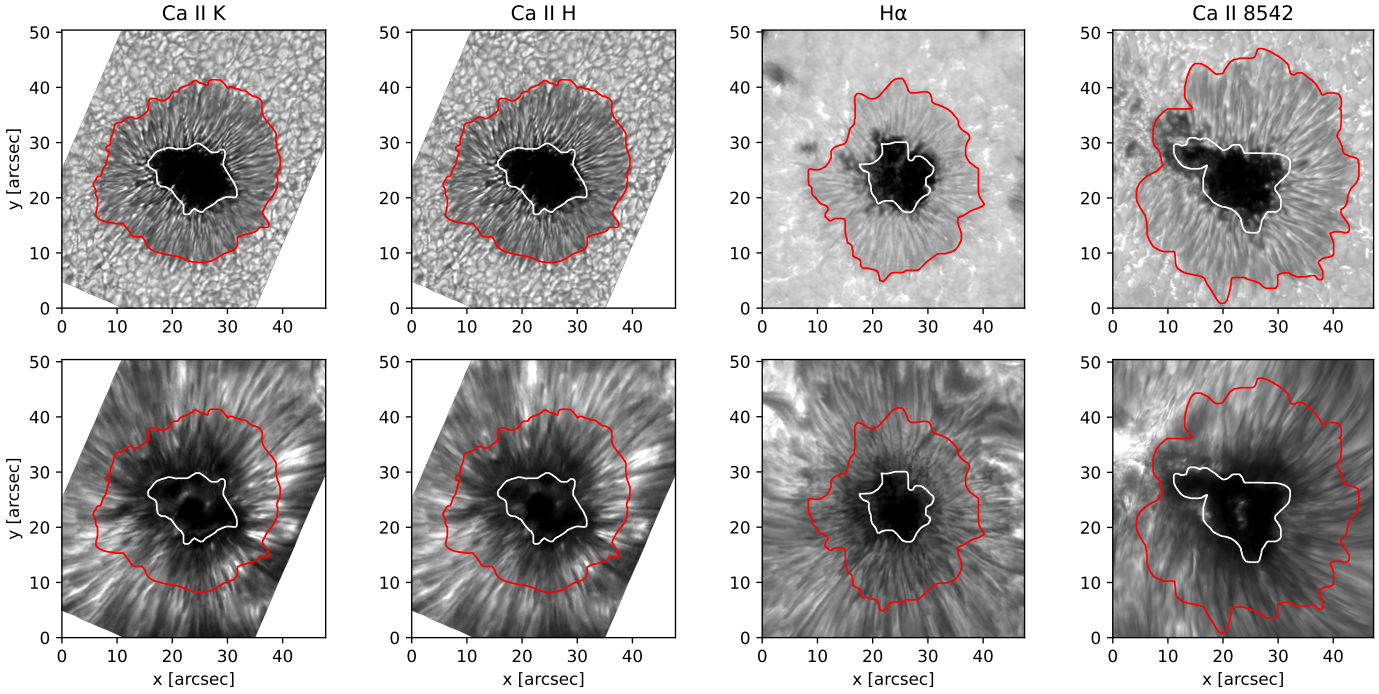

Fig. A.1. Sunspots used for the chromospheric-line analysis. *Upper panel:* Line-wing images showing the (pseudo-)photospheric appearance of the spots. Contours derived from intensity thresholds outline the umbra (white) and penumbra (red). *Lower panel:* Same fields of view shown in the respective line cores, probing the chromosphere at different heights. The same contours are overplotted to highlight the chromospheric contrast of the umbra, penumbra, and surrounding quiet Sun.

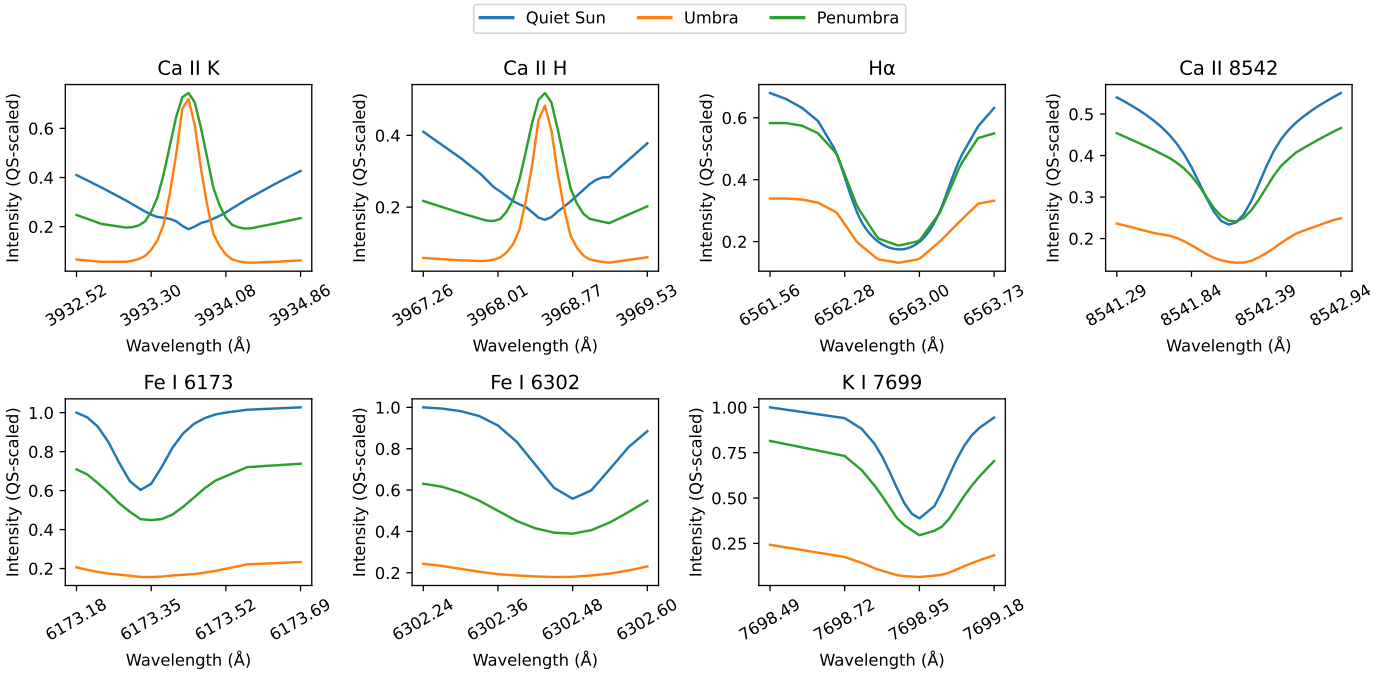

Fig. A.2. Resulting average profiles for quiet Sun (blue), penumbra (orange), and umbra (green) for eight spectral lines. For readability, all profiles are normalized to their respective quiet Sun profile.

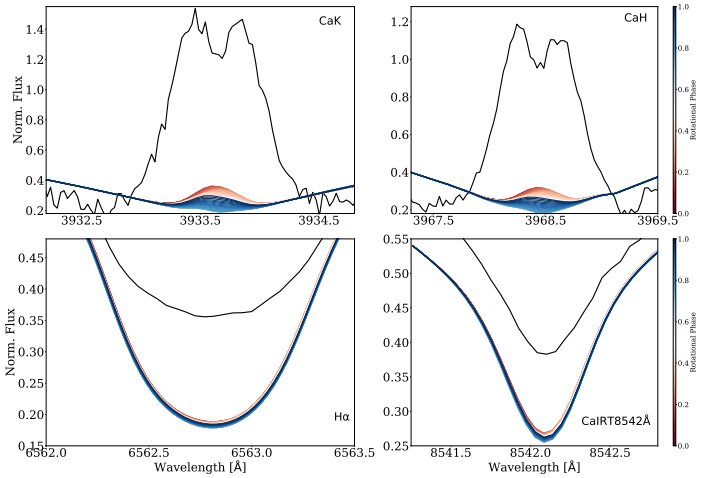

Fig. A.3. Color coded chromospheric emission lines compared with an observed profile at the median activity of λ And (black line).